

Faraday Discussions

Accepted Manuscript



This manuscript will be presented and discussed at a forthcoming Faraday Discussion meeting. All delegates can contribute to the discussion which will be included in the final volume.

Register now to attend! Full details of all upcoming meetings: <http://rsc.li/fd-upcoming-meetings>



This is an *Accepted Manuscript*, which has been through the Royal Society of Chemistry peer review process and has been accepted for publication.

Accepted Manuscripts are published online shortly after acceptance, before technical editing, formatting and proof reading. Using this free service, authors can make their results available to the community, in citable form, before we publish the edited article. We will replace this *Accepted Manuscript* with the edited and formatted *Advance Article* as soon as it is available.

You can find more information about *Accepted Manuscripts* in the [Information for Authors](#).

Please note that technical editing may introduce minor changes to the text and/or graphics, which may alter content. The journal's standard [Terms & Conditions](#) and the [Ethical guidelines](#) still apply. In no event shall the Royal Society of Chemistry be held responsible for any errors or omissions in this *Accepted Manuscript* or any consequences arising from the use of any information it contains.

SERS as a tool for *in vitro* toxicology

Kate M. Fisher,¹ Jennifer A. McLeish,² Lauren E Jamieson,¹ Jing Jiang,¹ James R Hopgood,³ Stephen McLaughlin,⁴ Ken Donaldson,² Colin J. Campbell¹

¹ EaStCHEM, School of Chemistry, University of Edinburgh, EH9 3FJ

² MRC Centre for Inflammation Research, ELEGI Colt Laboratory, Queen's Medical Research Institute, University of Edinburgh, EH16 4TJ

³ Institute for Digital Communications, Joint Research Institute for Signal and Image Processing, School of Engineering, University of Edinburgh, EH9 3JL

⁴ School of Engineering and Physical Sciences, Heriot Watt University, Edinburgh, EH14 4AS

Abstract

Measuring markers of stress such as pH and redox potential are important when studying toxicology in *in vitro* models because they are markers of oxidative stress, apoptosis and viability. While Surface Enhanced Raman Spectroscopy is ideally suited to the measurement of redox potential and pH in live cells, the time-intensive nature and perceived difficulty in signal analysis and interpretation can be a barrier to its broad uptake by the biological community.

In this paper we detail the development of signal processing and analysis algorithms that allow SERS spectra to be automatically processed so that the output of the processing is a pH or redox potential value.

By automating signal processing we were able to carry out a comparative evaluation of the toxicology of silver and zinc oxide nanoparticles and correlate our findings with qPCR analysis. The combination of these two analytical techniques sheds light on the differences in toxicology between these two materials from the perspective of oxidative stress.

Introduction

Redox potential is a function of the propensity of a chemical species to donate or accept electrons and the concentrations of the oxidised and reduced species. The Nernst equation allows the quantification of redox potentials under non-standard conditions:¹

$$E = E^{\circ} + \frac{RT}{nF} \ln \frac{[\text{Ox}]}{[\text{Red}]}$$

where E is the redox potential (V), E° is the standard redox potential (V), R is the universal gas constant ($\text{J K}^{-1} \text{mol}^{-1}$), T is the temperature (K), n is the number of electrons transferred, F is the Faraday constant (C mol^{-1}), $[\text{Ox}]$ is the concentration of oxidised species, and $[\text{Red}]$ is the concentration of reduced species.

Electron transfer drives energy transduction in biological cells. Electrons are transferred from reduced nicotinamide adenine dinucleotide (NADH) to molecular O_2 via a set of proteins that make up the electron transfer chain. As many functions of the cell are redox regulated (e.g. signalling; protein, DNA and RNA synthesis; and cell growth and death), the redox potential as defined by the Nernst equation clearly has

biological significance as it both controls and reflects the biological activity of cells.²⁻⁴

The overall redox potential of a cell can be viewed as the balance between the generation of reactive oxygen/nitrogen (ROS/RNS) species and the antioxidants that degrade them. Most ROS/RNS generation is endogenous, as by-products of respiration, protein folding and NADPH oxidase activity.⁵⁻⁷ Whilst some of these ROS/RNS species can cause harmful oxidation of biomolecules, some signalling pathways use these oxidised biomolecules to sense the redox status of the cell.⁸⁻¹⁰ Antioxidant enzymes or small molecules transfer electrons from thiol/disulphide redox couples to reduce/eliminate ROS/RNS and oxidised biomolecules; these couples are oxidised in the process and then re-reduced by accepting electrons from other species.¹¹⁻¹³

There are several thiol/disulphide redox couples in the cell. The main redox couple is glutathione/glutathione disulphide (GSH/GSSG) as it is mostly in the reduced form (GSH) and is the most abundant, with a concentration range of 1-11 mM.² The levels of GSH are therefore commonly used as a proxy for overall redox potential, however, it is important to note that there are many other redox couples in the cell that contribute to the overall intracellular redox potential. All of these redox couples are not necessarily in equilibrium with other each other, can vary independently of each other and are at different concentrations in different organelles.⁴

Dysregulation of redox potential occurs when antioxidant levels are overwhelmed by ROS/RNS levels, causing oxidative stress, which has been implicated in diseases such as chronic inflammation, cancer and neurodegeneration.¹³⁻¹⁵ Oxidative stress can modify protein function through irreversible oxidative modification of protein residues, affecting cell function through inhibition of signalling pathways and resulting in apoptosis.

The gold standard for ratiometric redox potential measurement is the use of roGFPs, a green fluorescent protein modified with redox-active surface cysteine residues.¹⁶ Each oxidation state of roGFP has a distinct excitation maximum, and a fluorescence measurement thus provides a ratio of oxidised to reduced species from which the redox potential can be calculated using the Nernst equation. However, roGFPs change oxidation state through interaction with glutaredoxins and this biases the measurement towards a measurement of GSH.¹⁷ As stated above, overall redox potential is not a single analyte but is the result of many redox couples.

Our approach bypasses the problems involved in calculating overall redox potential from these individual redox couples, by using surface-enhanced Raman spectroscopy (SERS). We have designed redox-active reporter molecules based on quinones, which are active over a wider range of redox potentials than roGFPs.¹⁸ These reporters change bond order depending on whether they are oxidised or reduced and these changes can be detected by Raman spectroscopy, thus allowing spectral discrimination between oxidised and reduced forms of the reporter molecule. Covalent attachment of our reporter molecules to gold nanoshells amplifies the Raman signal by up to 10^8 .^[19] The use of lower energy infrared wavelengths as compared to visible wavelengths minimises phototoxicity. Furthermore cell components autofluorescence at visible wavelengths but not at infrared wavelengths.

We have shown that nanoshells coated with our reporter molecules are taken up into the cytoplasm and are non-toxic in various cell lines. We have used our nanosensors to show the correlation between redox potential and caspase activity during apoptosis.¹⁸

In this paper we detail the development of spectral processing and analysis algorithms that allow SERS spectra to be automatically processed to give an output of redox potential. In general we think that such automated analysis will allow greater translation of SERS to biological problems and in this particular case, the automated analysis has allowed us to carry out a comparative evaluation of the oxidative stress cause by silver and zinc oxide nanoparticles and correlate our finding with qPCR analysis.

Experimental

Functionalisation of nanoshells (NS)

The nanoshells have a peak absorbance at ~780 nm, with an absorbance of 1 corresponding to 2.2×10^9 NS/ml. Absorbances were measured with a Cary 50 UV-Vis spectrophotometer and spectra recorded from 200–900 nm.

NQ-NS: 1–2 mg of 1,8-diaza-4,5-dithia-1,8-di(2-chloro-[1,4]-naphthoquinone-3-yl)octane (NQ) was dissolved in 100% ethanol, then heated and filtered before 10-fold dilution with sterile filtered water (Sigma Aldrich). The solution was then added to 2.2×10^9 gold nanoshells (Nanospectra Biosciences Ltd) and incubated overnight at room temperature. The nanoshells (NQ-NS) were then washed 3 times with sterile filtered water and the absorbance measured.

MBA-NS: 1-2 mg of *para*-mercapto benzoic acid (MBA) was dissolved in 100% ethanol, filtered and diluted 10-fold with sterile filtered water (Sigma Aldrich). The solution was then added to 2.2×10^9 gold nanoshells (Nanospectra Biosciences Ltd) and incubated overnight at room temperature. The nanoshells (MBA-NS) were then washed 3 times with sterile filtered water and the absorbance measured.

Cell culture

A549 cells were grown as monolayers in Dulbecco's modified Eagle's medium (DMEM), supplemented with 10% heat-inactivated foetal bovine serum (FBS), 10,000 units/ml penicillin/streptomycin and 200 mM L-glutamine (all Life Technologies) (complete medium). NQ-NS incubation was carried out in serum-free medium, i.e. complete medium lacking FBS. Cells were grown in an incubator at 37 °C with a humidified 5% CO₂ atmosphere.

Surface-enhanced Raman spectroscopy

Calibration data: MBA: Calibration data consisted of 3 independent datasets, each having 5 spectra per pH, making a total of 303 spectra, covering a range of 3.7 to 13.1 pH units. NQ: Calibration data consisted of 5 spectra per redox potential, making a total of 40 spectra, covering a range of -460 to -250 mV.

Preparation of cells: A549 cells were plated at a density of 2×10^5 cells/dish on 35 mm diameter glass-bottomed imaging dishes (Greiner Bio-One). The following day the medium was replaced with serum-free medium for 1.5 hours followed by overnight incubation with 200 fM NQ-NS. Cells were washed twice with PBS and 3 ml complete medium added. Cells were then either treated with 0.5 mg/ml silver nanoparticles (AgNP), 0.5 mg/ml zinc oxide nanoparticles (ZnONP) or 30 mM 2,2'-azobis(2-amidinopropane) dihydrochloride (AAPH; positive control) or were left untreated. Cells were incubated at 37 °C and 5% CO₂ until Raman spectroscopy was performed at 0, 1, 2, 3 and 4 hours after treatment. Spectra were acquired from each sample for 1 hour.

Spectra acquisition: Raman spectroscopy was performed with a Renishaw InVia Reflex microRaman spectrometer with a 785 nm diode laser. Spectra were acquired between a Stokes Raman shift range of 1350-1800 cm⁻¹. Single spectra were acquired with a 50× Olympus super long working distance objective (NA = 0.45) to give a focal diameter of 2.1 mm using a point focus lens, and a power density at the sample of 66 mW mm⁻². The integration time was 30 s unless specified otherwise. SERS maps from cells were obtained with a 50× Olympus super long working distance objective (NA = 0.45) to give a line with dimensions 24.95 × 2.1 mm using a line focus lens. Raster scans were performed with a computer controlled x,y-stage, a step size of 5 mm, an integration time of 3 s and a power density at the sample of 330 mW mm⁻². The co-ordinates of signals from nanosensors were recorded and further Raster scans were performed centred on these co-ordinates with a step size of 1 mm, an integration time of 30 s and a power density at the sample of 66 mW mm⁻².

Data analysis

Individual spectra were processed as univariate signals with unknown parameters, the parameters of which were estimated using customised algorithms implemented in MATLAB[®] to determine redox potential. Differences in redox potential between treatment groups and the negative control were tested using ANOVA followed by the Holm-Šidák multiple comparison test. The MATLAB[®] code used is available upon request.

qPCR analysis

Total cellular RNA was isolated from A549 cells using the NucleoSpin RNA II kit (Machery-Nagel) according to the manufacturer's instructions. RNA concentrations were measured using the NanoDrop 2000c Spectrophotometer (Thermo Scientific). RNA was converted to cDNA using High Capacity cDNA Reverse Transcription Kit (Applied Biosystems). qRT-PCR was performed using SYBR i-Taq SYBR Green Supermix with ROX (Bio-rad), 0.5 μg cDNA and primers for either 18S (F: 5'-CATGGATTCAACGCAGAAG, R: 5'-GTAAAGTTGTGCGTCTCTGC) or HO-1 (F: 5'-CCAGCAACAAAGTGCAAG, R: 5'-CACATGGCATAAAGCCCT). Cycling parameters were 95°C for 10 minutes, followed by 40 cycles of 95°C for 15 seconds and 60°C for 60 seconds. The specificity of PCR product was confirmed through melting point analysis and the relative abundance of mRNA was calculated by a standard curve method, with 18S rRNA as the reference gene.

Results

SERS maps containing hundreds of spectra from single cells can be acquired in a short space of time (one map can be obtained in less than 5 minutes). The individual spectra require processing in order to determine redox potential, which is a time-consuming process if done manually. First, the user must select those spectra with a sufficiently intense SERS spectrum to warrant further attention. A smoothing algorithm is then applied to each chosen spectrum, an individual manually specified baseline is then subtracted and the peak heights obtained from the maximum value in the range of each peak. This manual processing takes approximately 3 minutes per spectrum and even though not every individual spectrum will require processing, a significant amount of time is required to be invested for a single map. In the development of sensors it is usual to perform manual processing of data, due to the small data sets generated. However, application of the sensors to biological data, where large data sets are common requires automation of data processing.

There are a number of drawbacks to manual processing in addition to the length of time required:

- *Intra*-individual bias and variance - because the baseline is manually specified, differences in its placement can occur due to human error, fatigue, mood etc. It is also possible that the baseline is subconsciously placed in order to achieve the expected results.
- *Inter*-individual bias and variance - different people will specify the baseline slightly differently which could lead to small but systematic differences in peak height ratios. Furthermore, each person may have differing criteria for deciding which spectra should be processed, leading to possible differences in the average redox potential determined through the exclusion or inclusion of spectra with a lower signal to noise ratio (SNR).
- The smoothing algorithm maintains peak height, thus also maintaining the noise, so the measurement of peak height is affected by noise. The presence of spikes of noise on one peak and not the other leads to over- or under-estimation of peak height ratios.

All of the above mean that while SERS is an attractive technique for making pH and redox measurements in live cells, the challenges of data analysis provide a barrier to entry for life-scientists unfamiliar with vibrational spectroscopic data. Automating the process of data analysis addresses these drawbacks in addition to being faster. A univariate peak fitting approach was used to ascertain peak height, which has the advantage of being less affected by noise than the manual method, as well as removing the bias and variance inherent in manual processing as the same criteria are applied to all spectra. Peak fitting also allows the investigation of other parameters such as peak width and area, which may also change with redox potential or pH, offering more options for ratiometric analysis. Therefore peak fitting can provide a more accurate method of estimating redox potential or pH from SERS spectra.

Peak fitting is a common method of analysis in spectroscopy and chromatography as the peaks have characteristic shapes that can be modelled by specific functions.^{20,21} This allows a physical model to be tested, and data extracted from the model. The

function parameters can provide information on the physical properties of the analyte under investigation. For example, in Raman, fluorescence and UV-visible spectroscopy the intensity of a peak is proportional to concentration.²²

There are several examples of automated processing of Raman spectra in the literature, with most focusing on baseline subtraction to remove the large background signals from various sources, including autofluorescence from biological samples.²³⁻²⁶ For many applications, SERS spectral analysis is performed in order to detect/classify components of a sample,²⁷ and accurate peak finding can be problematic when dealing with an unknown number of peaks, especially overlapping ones.²⁰ However, the peaks in our SERS spectra are due solely to our reporter molecule and, furthermore, we are not interested in fitting all of the peaks in a spectrum but only those needed for a ratiometric measurement. Therefore the parameters of the peak fitting were constrained to produce a more accurate physical model.

Our preliminary algorithm development was carried out using the pH-sensitive MBA reporter molecule as it has well-separated peaks with relatively flat background between them.

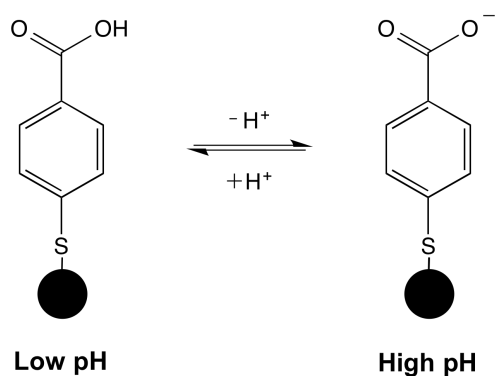


Figure 1: Structure of the MBA reporter molecule conjugated to a gold nanoshell (black circle) via a gold-thiol bond. The protonated form (left) predominates at low pH, whereas the deprotonated form (right) predominates at high pH.

The pH-sensitive *para*-mercaptobenzoic acid (MBA; Figure 1) molecule has been shown to be a good SERS-based reporter molecule for intracellular use.²⁸ Figure 2 shows how peaks in the spectrum change with pH: the peak at $\sim 1590\text{ cm}^{-1}$ is due to ring breathing;^{29,30} it is the most intense peak in the spectrum in the region $1300\text{--}1800\text{ cm}^{-1}$ and is therefore a good candidate for a reference peak, being present at both high and low pH. The centre of this peak can be seen to shift to lower wavenumbers as pH increases. The peak at $\sim 1400\text{ cm}^{-1}$ is barely distinguishable at low pH and increases as pH increases; it is due to COO^- stretching.²⁸⁻³⁰ At $\text{pH} > 8.5$ this peak moves to higher wavenumbers ($\sim 1420\text{ cm}^{-1}$) and becomes more intense. The peak at $\sim 1700\text{ cm}^{-1}$ shows the opposite trend: it is highest at low pH and decreases with increasing pH; it is due to C=O stretching.^{28,29} The opportunity therefore exists to use all three of these peak heights and areas in order to estimate pH, as well as the shift in centre of the 1590 cm^{-1} peak.

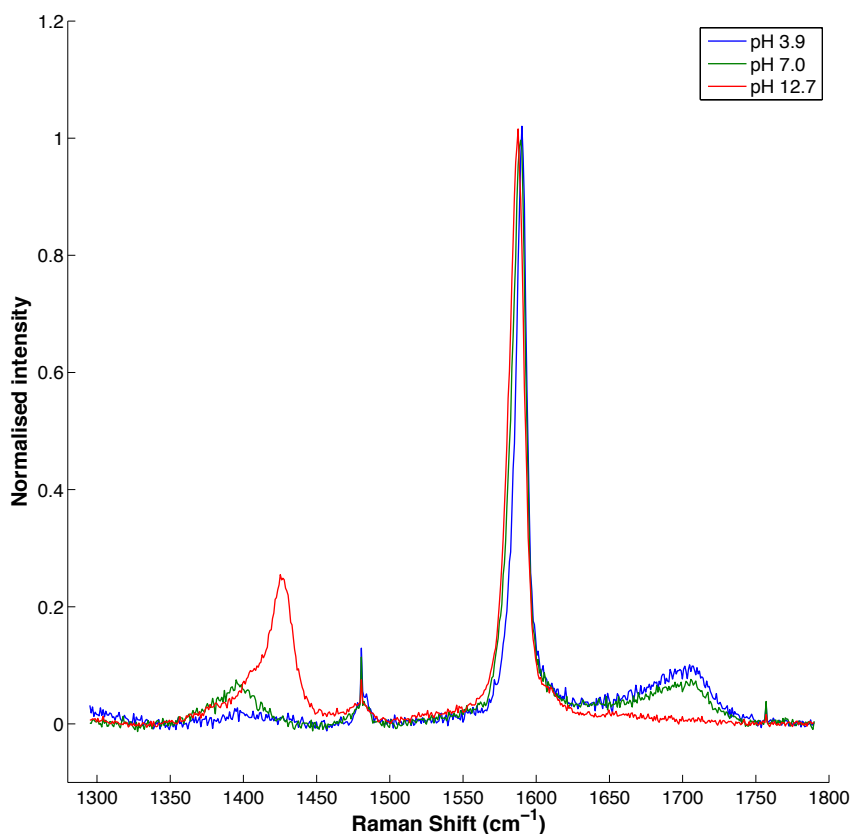


Figure 2: Change in the position and intensity of three peaks in the MBA-NS Raman spectrum as a function of pH. Spectra have been background subtracted and normalised to the intensity of the peak at $\sim 1590 \text{ cm}^{-1}$.

Peak fitting can either operate on univariate data as in this paper, or on an ensemble of spectra which can be analysed using multivariate methods such as independent component analysis. The univariate case is simpler to deal with, and is an exercise in classical curve fitting using an error criterion, for example such as least squares. In the univariate model, the peak shape can be modelled using a variety of functions, including Gaussian, Voigt, pseudo-Voigt, and asymmetric variants.²¹ However, the Lorentzian function is found to be the most parsimonious, requiring relatively few parameters, is simple to implement, and gives the least residual error.

Each of the three peaks in each spectrum is separately fitted around its peak centre using a Lorentzian peak model with an independent linear baseline:

$$y_n(x_c) = \frac{a_n}{1 + \left(\frac{x_c - b_n}{c_n}\right)^2} + m_n x_c + d_n$$

where $n \in \{1, \dots, P\}$ is the index of the n -th underlying spectral peaks, $P = 3$ is the number of spectral peaks, x_c is the Raman shift associated to the n -th peak, $y_n(x_c)$ is the normalised intensity of the n -th peak, a_n is the (positive) amplitude of the n -th peak, b_n is the peak centre, c_n is the peak width, m is the linear baseline gradient and d is the baseline offset.

The peak centres b_n are known *a priori*, whereas the unknown parameters a_n , c_n , m and d can be determined by the standard nonlinear least squares algorithm, using for example the Levenberg-Marquardt algorithm.³¹ This is implemented using the function “lsqcurvefit” in MATLAB. The Raman shift range over which each peak is fitted is determined experimentally as that which results in the least variation in the residuals over all the calibration spectra (excluding pH<6 for the peak at $\sim 1400\text{ cm}^{-1}$ and pH>8.5 for the peak at around $\sim 1700\text{ cm}^{-1}$). The same three ranges were then applied to all spectra. Figure 3 shows an example of a spectrum with each peak fitted separately. The peak width parameter, c_n , was constrained to be a minimum of 5 cm^{-1} and a maximum of 50 cm^{-1} (for the peak at $\sim 1590\text{ cm}^{-1}$) or 100 cm^{-1} (for the peaks at ~ 1400 and 1700 cm^{-1}) in case of very low SNR.

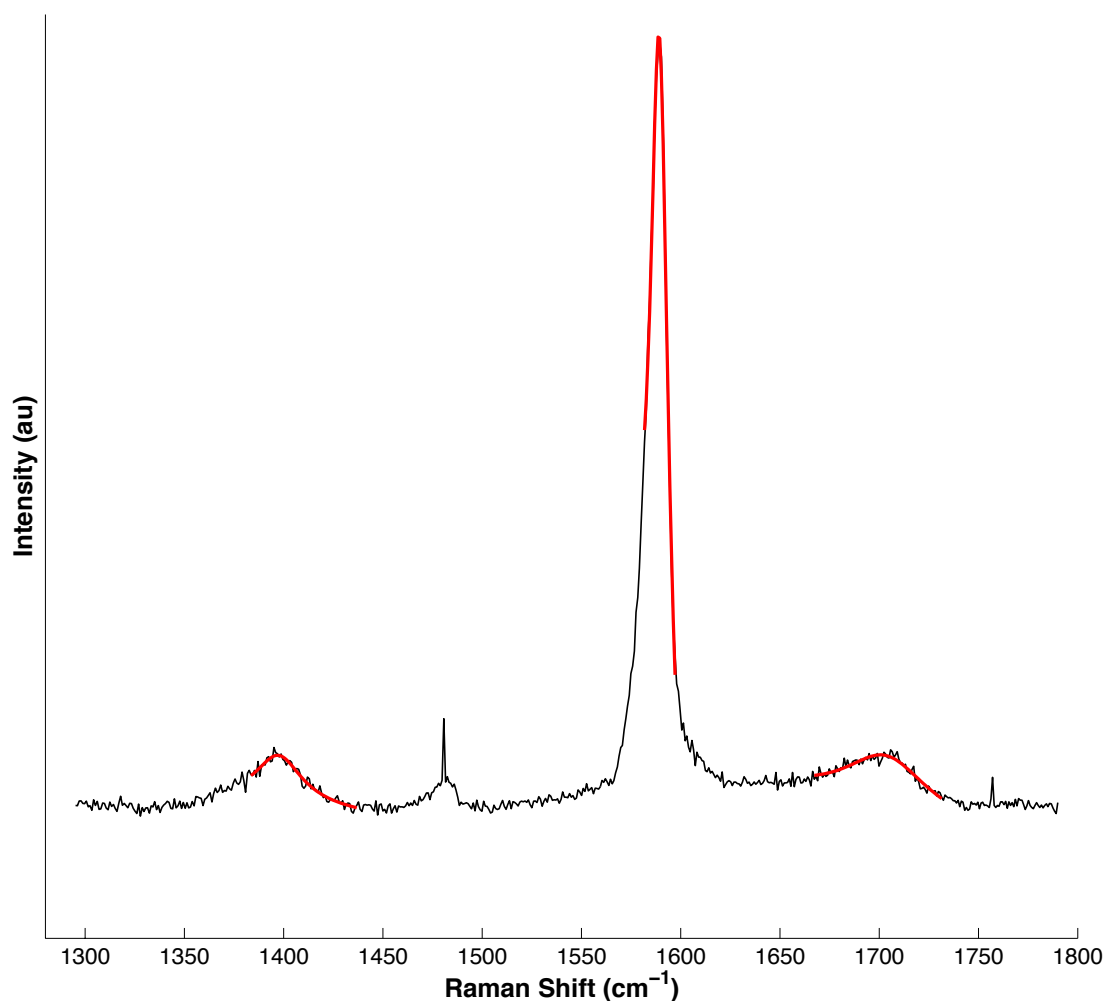


Figure 3: Example of a calibration spectrum (black) with peak fits applied to three separate regions (red). The Raman shift range of each fit was determined experimentally as that which resulted in the least variation in the residuals over all calibration data (excluding pH<6 for the peak at $\sim 1400\text{ cm}^{-1}$ and pH>8.5 for the peak at around $\sim 1700\text{ cm}^{-1}$).

The calibration data were grouped by pH in order to investigate relationships between various fit parameters and pH. Weighted means of the various parameters at each pH were calculated using inverse weighting to reduce the effect of values with a large error.

As expected, it was found that the centre of the peak at $\sim 1590\text{ cm}^{-1}$ did vary with pH, the centre of the peak at $\sim 1400\text{ cm}^{-1}$ shifted to higher wavenumbers at high pH, and the centre of the peak at $\sim 1700\text{ cm}^{-1}$ did not change with pH. The following ratios of peak heights and areas were dependent on pH: 1590/1400, 1590/1700 and 1400/1700, indicating that a combination of seven parameters ($\sim 1590\text{ cm}^{-1}$ peak centre, three peak height ratios and three peak area ratios) could be used to estimate pH.

The three datasets were combined, a Boltzmann curve fitted and the 95% confidence bands calculated for each of the seven parameters. Figure 4 shows the result of this fit for the change in the centre of the peak $\sim 1590\text{ cm}^{-1}$ (the other six parameters are shown in the Supplementary Material).

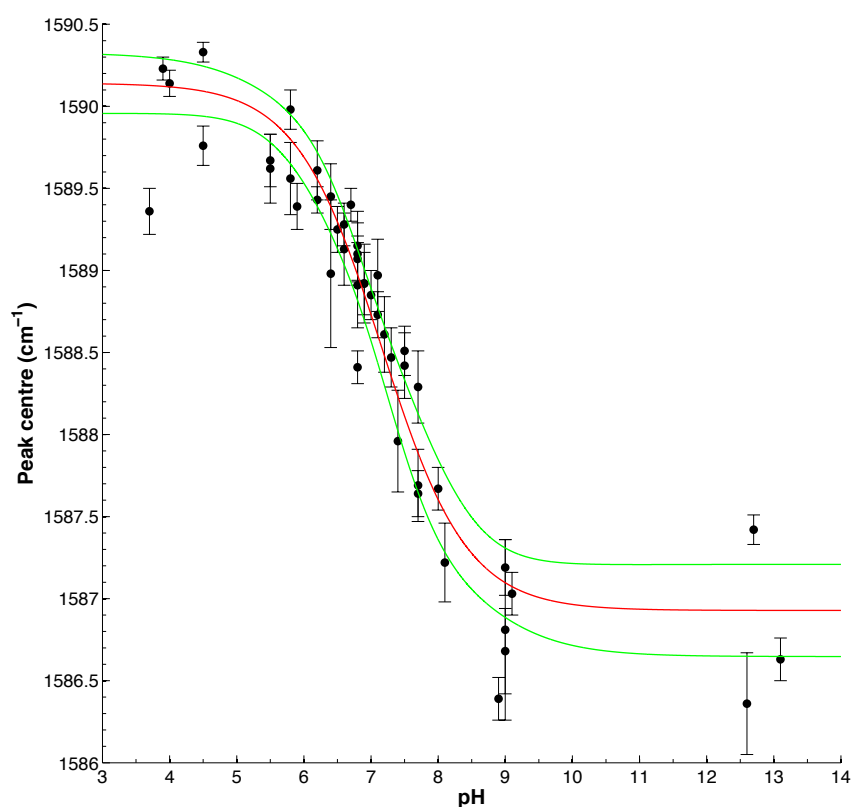


Figure 4: Variation of the centre of the peak at $\sim 1590\text{ cm}^{-1}$ with pH. A Boltzmann curve (red line) has been fitted to points which are the weighted means from three independent datasets; error bars are the standard deviation of the weighted mean; green lines are the 95% non-simultaneous confidence bands.

Figure 4 shows that the calibration is most accurate over a pH range of approximately 6-8; outside this range the estimated pH is subject to a large error. The aim of using this probe was to measure intracellular pH, which should be within this range, so acceptable ranges were therefore calculated for each parameter as the values of the Boltzmann fit at pH 6 and 8. The pH was then estimated from each of the seven calibration graphs, with an overall error in pH determined from both the error in the

Boltzmann fit and the error in the peak centre, height ratio or area ratio. The estimated pH from each parameter was combined into a weighted mean to give a more accurate estimate of pH. Spectra were marked as 'pH <6' or 'pH >8' as appropriate if they met either of the following conditions:

- if 2 or more area ratios were outside their acceptable ranges
- if 3 or more of the peak centre or height ratios were outside their acceptable ranges

These conditions ensure that at least four of the seven parameters are used to provide an estimate of pH. Using fewer than four parameters can result in a less accurate estimated value; therefore spectra with fewer than four parameters are marked as being outwith the range of the sensor.

When used to analyse the calibration data, this method resulted in an average standard deviation of ± 0.16 pH units. Individual 95% confidence intervals were calculated from the individual standard deviations of each spectrum, where the estimated pH was in the range 6-8; overall, 92.4% (very close to the expected value of 95%) of the calibration spectra were either correctly identified as being outwith the range of the sensor or the error range associated with the estimated pH contained the actual pH.

The automated algorithm was then compared to the manual processing method. The variability of spectra can be determined by acquiring consecutive spectra from the same aggregate of MBA-functionalised nanoshells dried onto a quartz coverslip. What is being tested is the variability between the manual and automatic processing methods, so it is important to obtain consecutive spectra that are very similar. To this end, 10 consecutive spectra were obtained from MBA-NS and processed by both methods. The manual process uses only one parameter to estimate pH: the ratio of the peak heights of the peaks at ~ 1400 and ~ 1590 cm^{-1} , whereas the automated process uses seven parameters. A comparison of the two methods is given in Figure 5 and Table 1. Manual processing of the 10 spectra resulted in a mean pH of 6.56 with a standard deviation of 0.29, whereas the automated processing resulted in a mean pH of 7.14 with a standard deviation of 0.09. The manual process does not provide an error associated with the estimated pH, whereas the automated process results in an associated mean error of 0.28 pH units. Furthermore, automated processing is nearly 200 times faster than manual processing and results in pH values spread evenly about the mean. The lower pH estimated by the manual method could be due to only using one parameter as the mean estimated pH of the same parameter by the automated method is 6.76 with a standard deviation of 0.21, lower than the mean derived from all seven parameters. These results show that not only is processing faster by two orders of magnitude, there is less variability in the automated processing method and the combination of seven parameters enables a more robust estimation of pH.

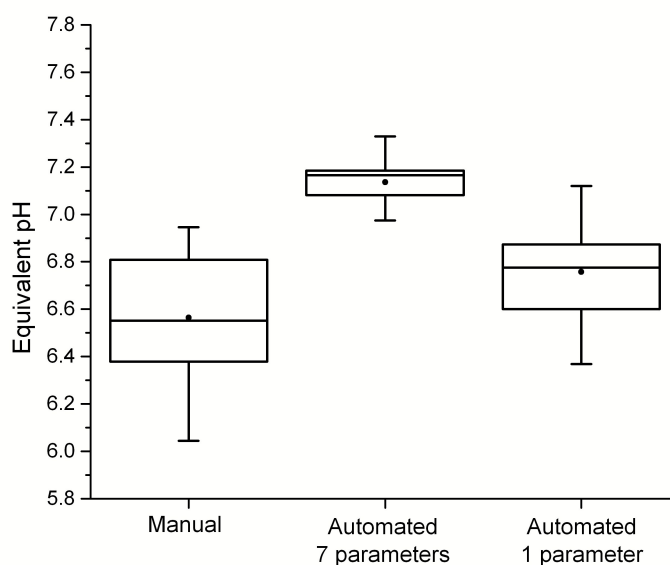


Figure 5: Boxplots showing the median, 1st and 3rd quarter percentiles, range and mean (filled circle) for the estimation of pH from 10 consecutive spectra obtained from MBA-NS using both manual and automated processing methods. The manual method uses only one parameter to estimate pH: the height ratio of the peaks at ~ 1400 and ~ 1590 cm^{-1} ; the pH estimated by the automated method using only this parameter is shown for comparison (Automated 1 parameter). The automated method uses a total of seven parameters to estimate pH and results in a much smaller range than the manual method.

	Manual processing	Automated processing
Mean estimated pH	6.56	7.14
Standard deviation	0.29	0.09
Mean error	-	0.28
Time per spectrum	3 minutes	1 second

Table 1: Comparison of manual and automated processing methods in the estimation of pH from 10 consecutive spectra obtained from MBA-NS. The manual method does not provide an error associated with the estimated pH. The automated method results in much less variation in estimated pH from each of the 10 spectra, and the processing time per spectrum is reduced by nearly 200-fold.

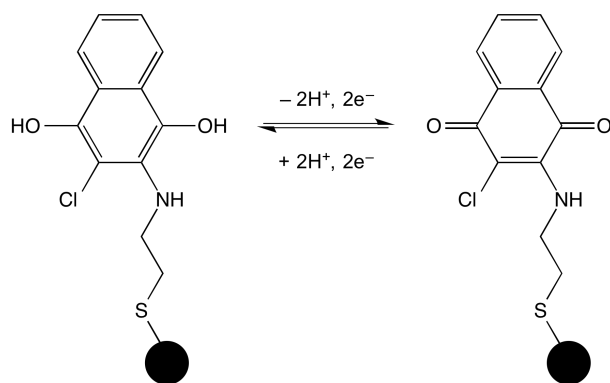


Figure 6: Reduced (left) and oxidised (right) structures of the NQ reporter molecule conjugated to a gold nanoshells (black circle) via a gold-thiol bond.

We used MBA-NS as a test-case for automated processing because the peaks used to measure pH are well resolved and easily identified. We then attempted to apply the same approach to automating redox potential measurement using the NQ-NS nanosensor developed in our lab (Figure 6).¹⁸ Figure 7 shows how peaks in the spectrum change with redox potential: the peak at $\sim 1580\text{ cm}^{-1}$ is actually composed of two peaks at 1577 cm^{-1} and 1602 cm^{-1} (symmetric ring breathing and aryl ring stretching with N-H wagging, respectively). This peak is the most intense peak in the region $1300\text{--}1800\text{ cm}^{-1}$, so it is a good candidate for the reference peak, whereas the peak at $\sim 1640\text{ cm}^{-1}$ is due to C=O stretching and can be used as a marker of increasing oxidation. For NQ, then, there is the possibility of using peak height and area ratios of a combination of the three peaks at 1577 cm^{-1} , 1602 cm^{-1} and 1640 cm^{-1} .

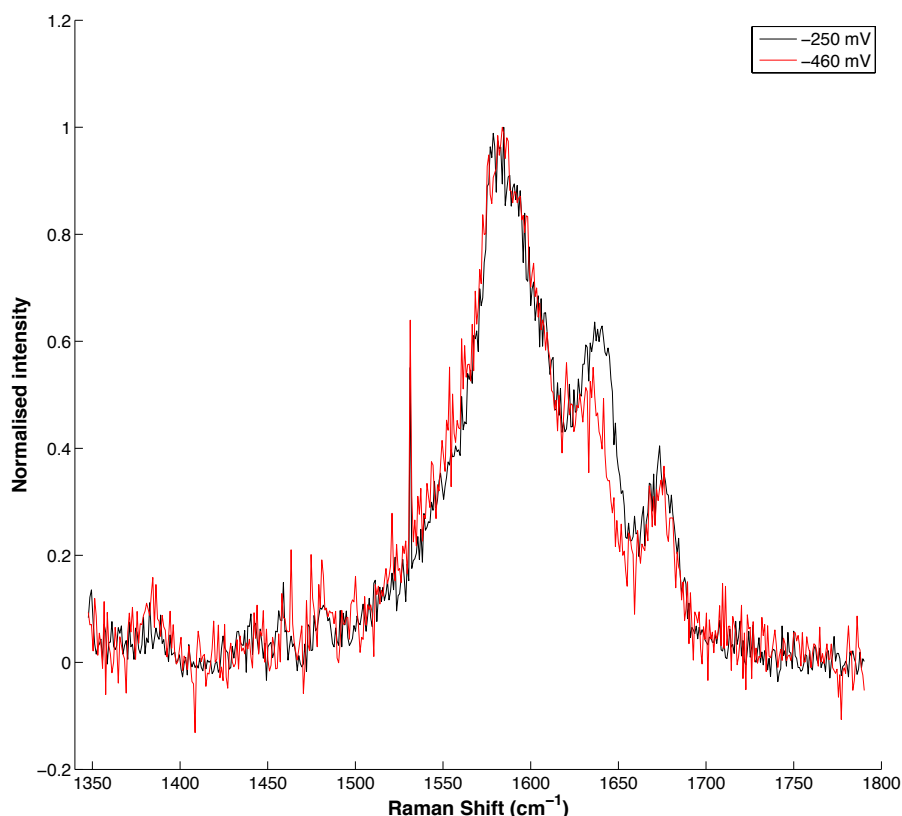


Figure 7: Redox-dependent change in the intensity of the peak at $\sim 1640 \text{ cm}^{-1}$ in the NQ-NS Raman spectrum. Spectra have been background subtracted and normalised to the intensity of the peak at 1577 cm^{-1} .

As the three peaks of interest overlapped, the data were modelled by the sum of three Lorentzian peaks:

$$y(x_c) = \sum_{n=1}^P \frac{a_n}{1 + \left(\frac{x_c - b_n}{c_n}\right)^2}$$

where again $n \in \{1, \dots, P\}$ is the index of the n -th underlying spectral peaks, $P = 3$ is the number of spectral peaks, x_c is the Raman shift, a_n is the (positive) amplitude of the n -th peak, b_n is the peak centre, and c_n is the peak width at 1577, 1602 and 1640 cm^{-1} , respectively. As discussed earlier, the amplitude and peak widths are estimated using a nonlinear least squares algorithm and the peak centres are known *a priori*. The Raman shift range over which the fit is applied is 1560-1660 cm^{-1} as this is the range that results in the least variation in the residuals over all calibration spectra. Constraints on peak widths were determined experimentally with a minimum of 40% and a maximum of 250% of the average peak width of the calibration spectra.

After fitting, the calibration data were grouped by redox potential in order to investigate relationships between various fit parameters and redox potential. The weighted means and standard deviations of the various parameters at each redox potential were calculated using the same inverse weighting method as for the MBA-NS nanosensor. It was found that the ratio of the height of the peaks at 1577 and $\sim 1640 \text{ cm}^{-1}$ varied with redox potential, as did the equivalent area ratios. The centres

of the peaks at 1577 and 1602 cm^{-1} did not change with redox potential, and the centre of the peak at $\sim 1640 \text{ cm}^{-1}$ only varied with redox potential at potentials more positive than -340 mV and thus could not be used to estimate redox potential. Therefore calibration curves were only constructed for the peak height and area ratios of the peaks at 1577 and $\sim 1640 \text{ cm}^{-1}$.

As before, a Boltzmann curve was fitted and 95% confidence bands were calculated for both of these parameters (Figure 8).

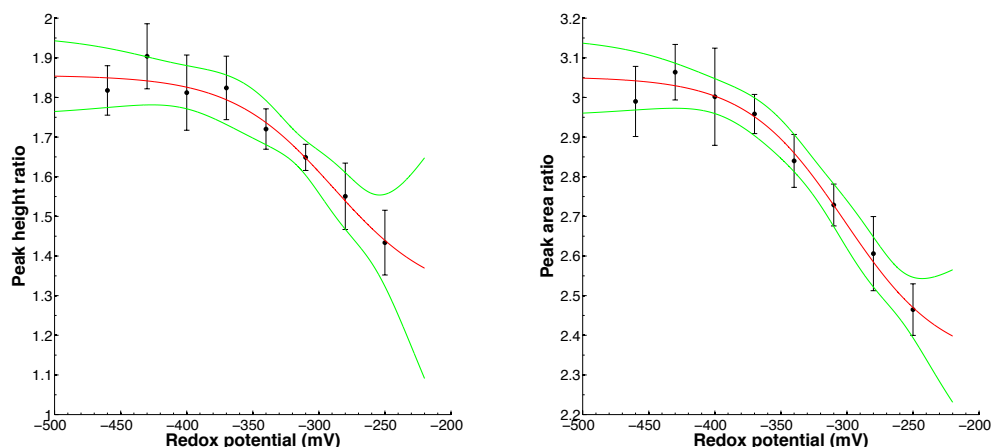


Figure 8: Variation of the 1577/1645 cm^{-1} peak height (top) and peak area (bottom) ratios with redox potential. A Boltzmann curve (red line) has been fitted to points which are the weighted means of five data points; error bars are the standard deviation of the weighted mean; green lines are the 95% non-simultaneous confidence bands.

Acceptable ranges for the ratios were calculated as the values at -400 and -250 mV, as this is the region where the curves change most rapidly. The redox potential was then estimated from both calibration graphs, with the overall error in redox potential determined from both the error in the Boltzmann fit and the error in the peak height or area ratio. With only two parameters used to estimate redox potential, there is a possibility that one parameter with a large error can skew the estimated redox potential away from the actual potential. Therefore the estimated redox potential from each parameter was combined into a weighted mean to avoid this effect. Spectra were marked as 'reduced' or 'oxidised' if either or both ratios were outside their acceptable ranges, and thus outwith the range of the sensor.

When used to analyse the calibration data, this method resulted in an average standard deviation of 23.3 mV. Individual 95% confidence intervals were calculated from the individual standard deviations of each spectrum, where the estimated redox potential was in the range -400 to -250 mV. Overall, 85% of the calibration spectra were either correctly identified as being outwith the range of the sensor or the error range associated with the estimated redox potential contained the actual redox potential. Obtaining more data would improve the accuracy of the weighted mean, and also improve the error in the calibration curve. In addition, data were collected at equally spaced redox potentials; due to the sigmoid shape of the calibration curve, this could mean a further loss of accuracy in the region of -350 to -250 mV where the slope is steepest. The 95% confidence intervals are greatest at more reducing potentials. This is due to the larger error in the height of the peak at 1640 cm^{-1} as it decreases with decreasing redox potential. This peak becomes a shoulder on the combined peaks at

1577 and 1602 cm^{-1} , resulting in increased error in the fit in this region at more reduced potentials. This error could be minimised by improving the SNR of the detector, but the problem can also be overcome by designing reporters with more reductive standard potentials^{32,33}.

The algorithm was then compared to the manual processing method. Ten consecutive spectra were obtained from NQ-NS dried onto an imaging dish and processed by both methods. The manual process uses only the peak height ratio, whereas the automated process uses both the peak height and area ratios. A comparison of the two methods is given in Table 2 and Figure 9. Manual processing of the 10 spectra results in a mean redox potential of -257.4 mV with a standard deviation of 3.0 mV, whereas the automated processing results in a mean redox potential of -259.3 mV with a standard deviation of 2.8 mV. The manual process does not provide an error associated with the estimated redox potential, whereas the automated process results in an associated mean error of 20.9 mV.

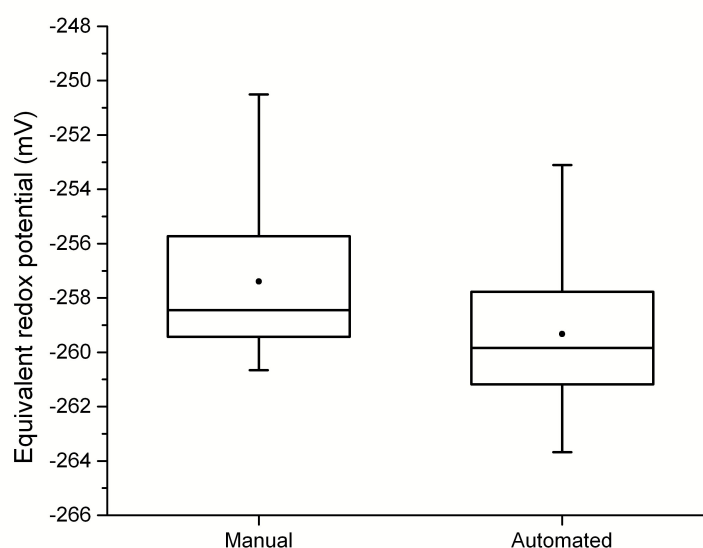


Figure 9: Box plots showing the median, 1st and 3rd quarter percentiles, range and mean (filled circle) for the estimation of redox potential from 10 consecutive spectra using both manual and automated processing methods.

	Manual processing	Automated processing
Mean estimated redox potential (mV)	-257.4	-259.3
Standard deviation (mV)	3.0	2.8
Mean error (mV)	-	20.9
Time per spectrum	3 minutes	1 second

Table 2: Comparison of manual and automated processing methods in the estimation of redox potential from 10 consecutive spectra obtained from NQ-NS. The manual processing method does not provide an error association with estimated redox potential. The automated processing method reduces the processing time per spectrum by nearly 200-fold.

The automated method was significantly faster than the manual method: nearly 200 times faster in processing a single spectrum, and 50-120 times faster in producing a colourmap of 147 spectra. The automated method was also more precise than the manual method for the MBA nanosensor and due to the lack of calibration spectra was no worse for the NQ nanosensor. However for the NQ nanosensor it was shown that the estimated values from the automated method were more evenly distributed about the mean than for the manual method, indicating that the automated method was less biased. All spectra were subject to the same criteria and intra- and inter-individual bias and variance were not present in the automated method.

Overall, the automated processing method is much faster and results in a less variable estimate of the pH or redox potential than the manual processing method.

Effect of zinc oxide and silver nanoparticles on redox potential

The toxicological effects of inhaled particulate matter have been extensively investigated. Inhalation of ultrafine particles, such as in diesel exhaust, has been shown to cause inflammation in several cell types.³⁴ The toxicity of these species is thought to be related to their large surface area to volume ratio, and/or their ability to act as a carrier of transition metals into the lungs.³⁵ Nanoparticles have a smaller diameter and greater surface area to volume ratio compared to larger particles and are now manufactured in large quantities for industrial use (for example, in the manufacture of cosmetics, electronics, and paint³⁶); therefore it is important to investigate the effects of nanoparticle inhalation during the manufacturing process. Engineered nanoparticles have been shown to have greater toxic effects than ultrafine particles (which are nanoscale ambient, as opposed to engineered, particles; for example air pollution particles), although the effects are strongly dependent on cell type.³⁴

As well as being used as a model of lung cancer,^{37,38} A549 cells are used in studies of inflammation³⁹ and nanoparticle toxicity^{35,40}. Both ultrafine particles and metal nanoparticles cause production of ROS in A549 cells.⁴¹ Elevated ROS levels cause upregulated expression of anti-oxidant genes through the Nrf2-KEAP pathway.⁴² At low particle concentrations this upregulation is enough to degrade ROS, however, at higher concentrations, the antioxidant response is insufficient for the levels of ROS produced, and the resulting oxidative stress triggers apoptosis.⁴³

This well-characterised response of A549 cells to nanoparticles makes them an ideal system in which to compare our measurements of intracellular redox potential with the traditional assays for oxidative stress.

A549 cells were incubated with NQ-NS overnight before either treatment with 30 mM 2,2'-azobis(2-amidinopropane) dihydrochloride (AAPH; positive control), sub-lethal treatment with one of 0.5 mg/ml silver nanoparticles (AgNP), 0.5 mg/ml zinc oxide nanoparticles (ZnONP) or were left untreated (see Experimental for full methods). SERS maps were acquired from untreated, AgNP-treated and ZnONP-treated cells over the following time periods after treatment: 0-1 hours; 1-2 hours; 2-3 hours; 3-4 hours and 4-5 hours. SERS spectra were acquired from AAPH-treated cells during the first hour after treatment only as there was extensive cell death after this period. Briefly, a cell or cells were rapidly scanned to locate any NQ-NS and then detailed scans covering an area of 6 x 25 mm were performed, centred on the location

of each NQ-NS signal from the rapid scan.

The automated processing algorithm described above was used to process all SER map spectra. After background subtraction, spectra were selected for further processing based on the following criteria:

- R^2 value ≥ 0.6
- height of the peak at $1577\text{ cm}^{-1} \geq 100$ counts

No spectra showed complete oxidation of NQ-NS. The automated processing method returned a redox potential with an associated error for each spectrum as described above. A weighted average and standard deviation was then calculated for each time period and each treatment, using the inverse weighting method. Figure 10 shows the change in redox potential for each time period for all treatments. In the 0-1 hour time period only AAPH-treated cells showed a significant oxidative shift in redox potential compared to untreated cells ($p = 0.0014$). In the 1-2 hour time period, both AgNP- and ZnONP-treated cells showed a significantly more oxidative redox potential compared to untreated cells ($p < 0.0001$ and $p = 0.0015$, respectively). For the other time periods there was no significant difference in redox potential between untreated cells and metal nanoparticle-treated cells.

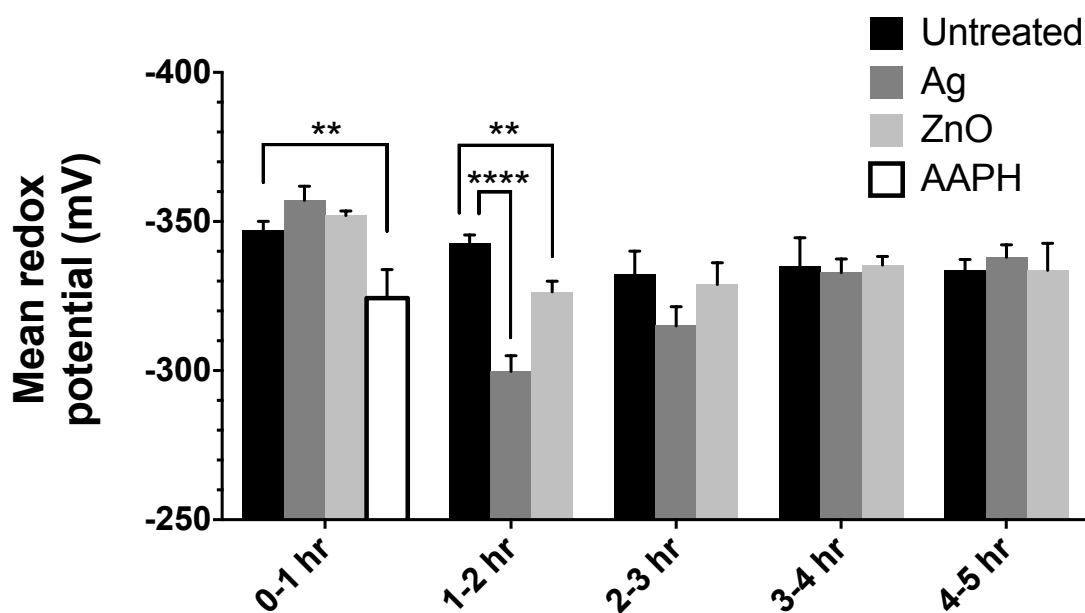


Figure 10: Metal nanoparticles increase intracellular redox potential in A549 cells 1-2 hours after treatment. Cells containing NQ-NS were treated with one of 0.5 mg/ml AgNP, 0.5 mg/ml ZnONP or 30 mM AAPH (positive control), or were left untreated. Bars show the weighted mean of redox potentials within each time period and treatment; error bars represent the standard error of the weighted mean; ** $p < 0.01$; **** $p < 0.0001$.

From Figure 10 it can be seen that both metal nanoparticle treatments showed the most oxidised redox potential during the 1-2 hour time period, with AgNP treatment resulting in a more oxidised potential than ZnONP treatment. All time periods showed significantly more positive redox potentials with respect to the potential measured during the 0-1 hour time period. In AgNP-treated cells, the redox potential during the

4-5 hour time period was significantly more reduced than the potential during the 1-2 hour or 2-3 hour time periods ($p = 0.0008$ and $p = 0.0208$, respectively), but it was still significantly more oxidised than during the 0-1 hour time period ($p = 0.0208$). ZnONP treatment showed the same trend but without reaching significance. The intracellular redox potential in untreated cells did not change significantly over the 5 hours.

These results were then compared to mRNA expression levels for selected antioxidant genes measured using qPCR. Nrf2 is a transcription factor that is responsive to changes in oxidative stress and an essential part of the cellular antioxidant response. Oxidative stress causes Nrf2 to translocate to the nucleus and upregulate expression of its target genes, many of which are antioxidants, including hemeoxygenase-1 (HO-1)⁴⁴. The levels of HO-1 mRNA transcripts were measured at three hours and showed that ZnONP, but not AgNP, treatment caused a significant upregulation of the HO-1 transcript (Figure 11). However, the concentration of AgNP at which only 50% of cells remained viable (TD₅₀) was much lower than for ZnONP (data not shown). Together, these data indicate that the less oxidative effect of ZnONP treatment could be due to an increase in antioxidant response, which is not seen with AgNP treatment.

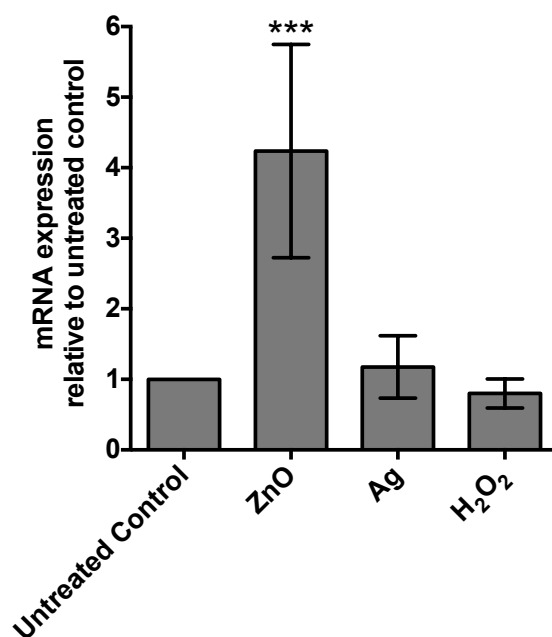


Figure 11: HO-1 mRNA expression 3 hours after treatment with metal nanoparticles in A549 cells.

Discussion and Conclusions

In this paper NQ-NS were used to measure the increase in intracellular redox potential in A549 cells treated with sub-lethal doses of engineered metal nanoparticles of Ag and ZnO, which have been shown to be toxic in A549 cells. The intracellular redox potential was shown to be most oxidised during the 1-2 hour time period for both metal NP treatments, with AgNP-treated cells showing more oxidised potentials than ZnONP-treated cells. ZnONP-treated cells showed upregulation of antioxidant genes compared to AgNP-treated cells and we speculate that the increased upregulation of

antioxidant genes seen in ZnONP-treated cells, compared to AgNP-treated cells, would enable metal NP-induced ROS to be degraded more efficiently and thus could explain the smaller increase in redox potential.

For both metal NP treatments, the intracellular redox potential returned to a value which was not significantly different to the untreated control population indicating that the cellular antioxidant response had reversed the effects of metal NP treatment on this timescale, in the surviving cells. In AgNP-treated cells, the redox potential became significantly more reductive after an initial oxidative shift, and eventually returned to a potential that is not significantly different to the untreated control cells. In ZnONP-treated cells this trend did not reach significance, perhaps due to increased upregulation of anti-oxidant genes.

In summary, our SERS nanosensor method of measuring intracellular redox potential is capable of measuring differences in oxidative stress caused by nanoparticles in A549 cells, and is corroborated by traditional assays of oxidative stress.

1. Fisher AC. *Electrode Dynamics*. Oxford University Press; 1996.
2. Schafer F, Buettner G. Redox environment of the cell as viewed through the redox state of the glutathione disulfide/glutathione couple. *Free Radic Biol Med*. 2001;30(11):1191–212.
3. Menon SG, Goswami PC. A redox cycle within the cell cycle: ring in the old with the new. *Oncogene*. 2007 Feb 22;26(8):1101–9.
4. Kemp M, Go Y-M, Jones DP. Nonequilibrium thermodynamics of thiol/disulfide redox systems: a perspective on redox systems biology. *Free Radic Biol Med*. 2008 Mar 15;44(6):921–37.
5. Berg JM, Tymoczko JL, Stryer L. *Biochemistry*. 6 ed. New York: W.H. Freeman and Company; 2007.
6. Bedard K, Krause K-H. The NOX family of ROS-generating NADPH oxidases: physiology and pathophysiology. *Physiol Rev*. 2007 Jan;87(1):245–313.
7. Pollard MG, Travers KJ, Weissman JS. Ero1p: a novel and ubiquitous protein with an essential role in oxidative protein folding in the endoplasmic reticulum. *Molecular Cell*. 1998 Jan;1(2):171–82.
8. Janssen-Heininger YMW, Mossman BT, Heintz NH, Forman HJ, Kalyanaraman B, Finkel T, et al. Redox-based regulation of signal transduction: principles, pitfalls, and promises. *Free Radic Biol Med*. 2008 Jul 1;45(1):1–17.
9. Winterbourn CC. Reconciling the chemistry and biology of reactive oxygen species. *Nat Chem Biol*. 2008 May;4(5):278–86.
10. Finkel T. Signal transduction by reactive oxygen species. *J Cell Biol*. 2011 Jul

- 11;194(1):7–15.
11. Nordberg J, Arnér ES. Reactive oxygen species, antioxidants, and the mammalian thioredoxin system. *Free Radic Biol Med*. 2001 Dec 1;31(11):1287–312.
 12. Mates J. Effects of antioxidant enzymes in the molecular control of reactive oxygen species toxicology. *Toxicology*. 2000;153(1):83–104.
 13. Dröge W. Free radicals in the physiological control of cell function. *Physiol Rev*. 2002 Jan;82(1):47–95.
 14. Andersen JK. Oxidative stress in neurodegeneration: cause or consequence? *Nat Med*. 2004 Jul;10 Suppl:S18–25.
 15. Valko M, Leibfritz D, Moncol J, Cronin MTD, Mazur M, Telser J. Free radicals and antioxidants in normal physiological functions and human disease. *The International Journal of Biochemistry & Cell Biology*. 2007;39(1):44–84.
 16. Dooley CT, Dore TM, Hanson GT, Jackson WC, Remington SJ, Tsien RY. Imaging dynamic redox changes in mammalian cells with green fluorescent protein indicators. *J Biol Chem*. 2004 May 21;279(21):22284–93.
 17. Meyer AJ, Brach T, Marty L, Kreye S, Rouhier N, Jacquot J-P, et al. Redox-sensitive GFP in *Arabidopsis thaliana* is a quantitative biosensor for the redox potential of the cellular glutathione redox buffer. *Plant J*. 2007;52(5):973–86.
 18. Auchincloss CAR, Richardson P, McGuinness C, Mallikarjun V, Donaldson K, McNab H, et al. Monitoring intracellular redox potential changes using SERS nanosensors. *ACS Nano*. 2012 Jan 24;6(1):888–96.
 19. Bantz KC, Meyer AF, Wittenberg NJ, Im H, Kurtuluş Ö, Lee SH, et al. Recent progress in SERS biosensing. *Phys Chem Chem Phys*. 2011 Jun 28;13(24):11551–67.
 20. Maddams WF. The scope and limitations of curve fitting. *Applied Spectroscopy*. 1980;34(3):245–67.
 21. Di Marco VB, Bombi GG. Mathematical functions for the representation of chromatographic peaks. *J Chromatogr A*. 2001 Oct 5;931(1-2):1–30.
 22. Robinson JW, EM SF, Frame GM II. *Undergraduate Instrumental Analysis*. Sixth. Marcel Dekker; 2005.
 23. Zhao J, Lui H, McLean DI, Zeng H. Automated autofluorescence background subtraction algorithm for biomedical Raman spectroscopy. *Applied Spectroscopy*. 2007 Nov;61(11):1225–32.
 24. Beattie JR. Optimising reproducibility in low quality signals without smoothing; an alternative paradigm for signal processing. *J Raman Spectrosc*. Wiley Online Library; 2011;42(6):1419–27.

25. Schulze HG, Foist RB, Okuda K, Ivanov A, Turner RFB. A model-free, fully automated baseline-removal method for Raman spectra. *Applied Spectroscopy*. 2011 Jan;65(1):75–84.
26. Lau SK, Winlove P, Moger J, Champion OL, Titball RW, Yang ZH, et al. A Bayesian Whittaker-Henderson smoother for general-purpose and sample-based spectral baseline estimation and peak extraction. *J Raman Spectrosc*. Wiley Online Library; 2012;43(9):1299–305.
27. Sharma B, Frontiera RR, Henry A-I, Ringe E, Van Duyne RP. SERS: materials, applications, and the future. *Materials Today*. Elsevier; 2012;15(1):16–25.
28. Bishnoi SW, Rozell CJ, Levin CS, Gheith MK, Johnson BR, Johnson DH, et al. All-optical nanoscale pH meter. *Nano Lett*. 2006 Aug;6(8):1687–92.
29. Kneipp J, Kneipp H, Wittig B, Kneipp K. One- and two-photon excited optical pH probing for cells using surface-enhanced Raman and hyper-Raman nanosensors. *Nano Lett*. 2007 Sep;7(9):2819–23.
30. Ochsenkuhn MA, Jess PRT, Stoquert H, Dholakia K, Campbell CJ. Nanoshells for Surface-Enhanced Raman Spectroscopy in Eukaryotic Cells: Cellular Response and Sensor Development. *ACS Nano*. 2009;3(11):3613–21.
31. Marquardt DW. An algorithm for least-squares estimation of nonlinear parameters. *Journal of the Society for Industrial & Applied ...* 1963.
32. Jiang J, Auchinvole C, Fisher K, Campbell CJ. Quantitative measurement of redox potential in hypoxic cells using SERS nanosensors. *Nanoscale*. 2014 Oct 21;6(20):12104–10.
33. Thomson P, Camus VL, Hu Y, Campbell CJ. Series of Quinone-Containing Nanosensors for Biologically Relevant Redox Potential Determination by Surface-Enhanced Raman Spectroscopy. *Anal Chem*. 2015.
34. Stone V, Johnston H, Clift M. Air pollution, ultrafine and nanoparticle toxicology: cellular and molecular interactions. *IEEE Transactions on Nanobioscience*. 2007;6(4):331–40.
35. Brown D, Wilson M, MacNee W, Stone V, Donaldson K. Size-dependent proinflammatory effects of ultrafine polystyrene particles: A role for surface area and oxidative stress in the enhanced activity of ultrafines. *Toxicol Appl Pharm*. 2001;175(3):191–9.
36. Vandebriel RJ, De Jong WH. A review of mammalian toxicity of ZnO nanoparticles. *Nanotechnol Sci Appl*. 2012;5:61–71.
37. Jeon S-M, Chandel NS, Hay N. AMPK regulates NADPH homeostasis to promote tumour cell survival during energy stress. *Nature*. 2012 May 31;485(7400):661–5.
38. Kim TR, Cho EW, Paik SG, Kim IG. Hypoxia-induced SM22 alpha in A549

- cells activates the IGF1R/PI3K/Akt pathway, conferring cellular resistance against chemo- and radiation therapy. *FEBS Lett.* 2012;586(4):303–9.
39. Standiford TJ, Kunkel SL, Basha MA, Chensue SW, Lynch JP, Toews GB, et al. Interleukin-8 gene expression by a pulmonary epithelial cell line. A model for cytokine networks in the lung. *J Clin Invest.* 1990 Dec;86(6):1945–53.
 40. Simon-Deckers A, Gouget B, Mayne-L'hermite M, Herlin-Boime N, Reynaud C, Carrière M. In vitro investigation of oxide nanoparticle and carbon nanotube toxicity and intracellular accumulation in A549 human pneumocytes. *Toxicology.* 2008 Nov 20;253(1-3):137–46.
 41. Lu S, Zhang W, Zhang R, Liu P, Wang Q, Shang Y, et al. Comparison of cellular toxicity caused by ambient ultrafine particles and engineered metal oxide nanoparticles. *Part Fibre Toxicol.* 2015;12(1):5.
 42. Deng X, Zhang F, Rui W, Long F, Wang L, Feng Z, et al. PM2.5-induced oxidative stress triggers autophagy in human lung epithelial A549 cells. *Toxicol In Vitro.* 2013 Sep;27(6):1762–70.
 43. Pisani C, Gaillard J-C, Nouvel V, Odorico M, Armengaud J, Prat O. High-throughput, quantitative assessment of the effects of low-dose silica nanoparticles on lung cells: grasping complex toxicity with a great depth of field. *BMC Genomics.* 2015;16:315.
 44. Thimmulappa RK, Mai KH, Srisuma S, Kensler TW, Yamamoto M, Biswal S. Identification of Nrf2-regulated genes induced by the chemopreventive agent sulforaphane by oligonucleotide microarray. *Cancer Res.* 2002 Sep 15;62(18):5196–203.